Journal of Alloys and Compounds 871 (2021) 159525

Contents lists available at ScienceDirect

Journal of Alloys and Compounds

journal homepage: www.elsevier.com/locate/jalcom

Lattice dynamics study of $(Gd_{1-x}Yb_x)_2O_3$(x=0.11) at high pressure

Julia Marí-Guaita[a,*], S. Gallego-Parra[a], J.A. Sans[a], M. Velázquez[b], Philippe Veber[c], P. Rodríguez-Hernández[d], A. Muñoz[d], F.J. Manjón[a,*]

[a] Instituto de Diseño para la Fabricación y Producción Automatizada, MALTA Consolider Team, Universitat Politècnica de València, 46022 València, Spain
[b] Univ. Grenoble Alpes, CNRS, Grenoble INP, SIMAP, 38000 Grenoble, France
[c] CNRS, Institut Lumière Matière, Université Claude Bernard Lyon 1, UMR5306, 69622 Villeurbanne, France
[d] Departamento de Física, Instituto de Materiales y Nanotecnología, MALTA Consolider Team, Universidad de La Laguna, 38207 San Cristóbal de La Laguna, Spain

ARTICLE INFO

Article history:
Received 14 December 2020
Received in revised form 10 March 2021
Accepted 11 March 2021
Available online 15 March 2021

Keywords:
High pressure
Raman spectroscopy
Rare earth sesquioxides
$(Gd_{1-x}Yb_x)_2O_3$

ABSTRACT

In this study, we report an experimental investigation of $(Gd_{1-x}Yb_x)_2O_3$ under high pressure by means of Raman scattering measurements complemented with *ab initio* calculations in pure Gd_2O_3. Raman spectroscopy of compressed $(Gd_{1-x}Yb_x)_2O_3$ (x = 0.11) revealed a first phase transition from the cubic $Ia\bar{3}$ phase (C-type) to the monoclinic *C2/m* phase (B-type) at 6.2 GPa followed by a second phase transition towards the trigonal $P\bar{3}m1$ phase (A-type) at 9.8 GPa. This sequence of phase transitions is different to that previously reported for pure Gd_2O_3. A phase transition from the trigonal to the monoclinic phase is observed on downstroke, so the B-type phase remains metastable at room pressure, as observed in all C-type rare earth sesquioxides. Theoretical calculations have helped to identify the different polymorphs and to assign the symmetry of the observed first-order Raman-active modes in the three phases. The pressure coefficients of the Raman-active modes of the three phases followed under pressure have been reported and compared to those of pure Gd_2O_3 and other rare-earth sesquioxides.

1. Introduction

Rare-earth (*RE*) sesquioxides (SOs) are oxides of the chemical elements with atomic numbers 57–71 (for lanthanides) and 89–103 (for actinides). *RE* SOs have RE_2O_3 stoichiometry and have been studied for many years because of their large interest in scientific and technological fields. These compounds show great applications as light emitters (lasers and improved phosphors), catalysts, high-dielectric constant (high-k) gates, neutron absorber for nuclear fuel control, nuclear waste storage, data storage, magnetorestrictive alloys, magnetic refrigeration, cement additives, paints, coatings, solid oxide fuel cells, etc [1]. From all the RE_2O_3 compounds, Gd_2O_3 exhibits an attractive and potential applications in many fields of technology. It is used as corrosion resistive and passivating coating because of its high refractive index [2] and it is very useful when used as antireflection coating. Also, when doped with rare-earth ions, Gd_2O_3 shows good luminescent properties. In particular, notable interest has been recently found in the luminescent properties and laser operation of Yb-doped Gd_2O_3 [3–6].

RE_2O_3 compounds can be found at ambient conditions depending on the ionic radius of the *RE* element in either of three phases [7]: the trigonal A-type structure (space group (s.g.) $P\bar{3}m1$, No. 164), the monoclinic B-type structure (s.g. *C2/m*, No. 12) and the cubic C-type structure (s.g. $Ia\bar{3}$, No. 206). The molar volume of *RE* SOs is known to decrease in the sequence C→B→A with increasing cation coordination number at ambient conditions. Then, high pressure (HP) is expected to cause the sequence (C→B→A)[8]. In particular, Gd_2O_3 has been synthesized in the cubic and monoclinic phases at ambient conditions and transformation between the B and C phases has been found at high temperatures [7]. The unit cell of cubic C-type Gd_2O_3 (Fig. 1 (left)) contains three independent atoms: two inequivalent Gd^{3+} atoms, located at 8*b* and at 24*d* Wyckoff sites, and one O^{2-} atom located at a 48*e* site. In this phase, both Gd^{3+}cations are surrounded by six O^{2-} anions. The unit-cell of monoclinic B-type Gd_2O_3 (Fig. 1 (center)) contains eight independent atoms: three Gd^{3+} located at 4*i* Wyckoff sites and five O^{2-}, four of them located at 4*i* Wyckoff sites and one located at a 2*b* site. In this phase one Gd atom is coordinated with 6O atoms and two Gd atoms are coordinated with 7O atoms. Finally, the unit-cell of trigonal A-type Gd_2O_3 observed at HP (Fig. 1 (right)) contains three independent atoms: one Gd^{3+} located in a *2d* Wyckoff position and two O^{2-} located in *1a* and *2d* Wyckoff positions. In this phase, Gd^{3+} is sevenfold coordinated to O^{2-}.

* Corresponding author.
E-mail addresses: juliasetze@gmail.com (J. Marí-Guaita), fjmanjon@fis.upv.es (F.J. Manjón).

https://doi.org/10.1016/j.jallcom.2021.159525
0925-8388/

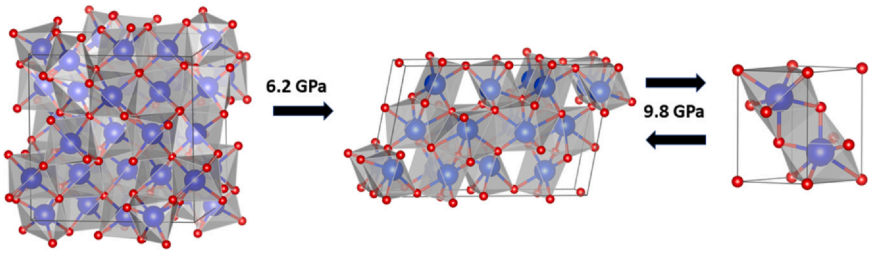

Fig. 1. Scheme of the phase transition sequence observed in $Gd_{1.78}Yb_{0.22}O_3$. (Left) Cubic C-type s.g $Ia\bar{3}$ (Center) Monoclinic B-type s.g $C2/m$ and (Right) Trigonal A-type s.g $P\bar{3}m1$.

The Raman scattering of Gd_2O_3 has been studied in several works either in the C- or B-type phases at room pressure [9–19]. Up to 19 modes out of 22 were observed for C-type Gd_2O_3 and up to 21 modes out of 21 were observed for B-type Gd_2O_3 [13]. Theoretical first-principle studies of the structural, elastic, and electronic properties of *RE* sesquioxides in the A, B, and C-type phases have been reported [20–38], but a theoretical study of the vibrational properties of any of their three phases has only been performed for local vibrational modes of Eu and Yb in Gd_2O_3 [39,40] and more recently for Tb_2O_3 [41]. Therefore, no theoretical first-principles study of the vibrational properties of Gd_2O_3 is available in the literature to our knowledge.

Several studies have been devoted to Gd_2O_3 under compression from an experimental point of view using either X-ray diffraction (XRD), Raman scattering (RS) or photoluminescence (PL) measurements and *ab initio* calculations [42–54]. In a first study, C-type Gd_2O_3 was shock-loaded to 2–50 GPa, thus transforming Gd_2O_3 into the B-type structure according to XRD measurements [42]. In a subsequent work, C-type Gd_2O_3 was shown to transform directly to the trigonal A-type structure between 4.6 and 5.2 GPa according to HP-XRD measurements under static compression and the B-type structure was found on downstroke below 5.2 GPa [43]. More recently, bulk and nanocrystalline (30 nm) Eu^{3+}-doped Gd_2O_3 was studied by HP-XRD and HP-PL measurements that found the C-A phase transition (PT) above 13.4 GPa, irrespective of the grain size and the obtention of the B phase was confirmed on downstroke [44,45]. Later, HP-XRD measurements confirmed the C-A PT on upstroke and gave the bulk moduli of both phases [46]. The C-A transition between 7.0 and 15 GPa and the recovery of the B phase on downstroke was also confirmed by Zhang et al. in bulk Gd_2O_3 both by HP-XRD and HP-RS measurements [47]. Besides, the bulk modulus of bulk C-type Gd_2O_3 was provided. Unfortunately, neither the Raman-active modes of the C-type phase under compression, nor the Raman-active modes of the HP phases were followed except for two modes of the A phase near 500 cm^{-1} at HP, nor the characterization of the RS spectrum of the B-type phase at room pressure has been observed. Up to five Raman-active modes of the C-type phase were measured at HP by Dilawar et al. in Gd_2O_3 30-nm nanocrystals [48]; however, the nanocrystals showed a pressure-induced amorphization (PIA) above 9 GPa since the two modes of the trigonal phase near 500 cm^{-1} were observed to be on top of a very broad band, likely due to amorphous material. Further HP-XRD measurements in bulk Gd_2O_3 reported a C-B PT on the sample loading process, due to precompression of powders to around 2 GPa. This PT was followed by a B-A PT above 8.9 GPa [49], which would indicate the sensitivity of this compound to non-hydrostatic conditions. Moreover, the bulk moduli of the three phases were provided and compared to theoretical calculations. Similarly, HP-XRD measurements in bulk Gd_2O_3 reported the C-A PT on upstroke above 7.0 GPa and the bulk moduli of the two phases was reported [50]. More recently, HP-XRD measurements were also used to study the effect of Er doping on the Gd_2O_3 PT sequence [51]. The C-A PT was found above 8.6 GPa on upstroke and the B-type phase was found below 9.5 GPa on downstroke. Besides, the bulk moduli of the three phases were provided and compared to those provided by previous works. Further, HP-PL and HP-RS measurements were performed in Eu^{3+}-doped Gd_2O_3 nanorods [52], showing the C-A PT above 11.3 GPa. Again, very few Raman-active modes of the C- and A-type phases were followed at HP and no detail analysis of the lattice dynamics was done as in previous papers. HP-XRD and HP-RS measurements were used to study C-type Er^{3+}-doped Gd_2O_3 nanorods [53]. A PIA above 9.4 GPa was found and a bulk modulus much larger than that of the bulk material was found despite having a similar but slightly larger lattice parameter. Finally, HP-RS measurements in C-type Gd_2O_3 nanocrystals reported the pressure dependence of the most intense Raman-active mode. These modes were compared to those of nanocrystals of other C-type *RE* sesquioxides, finding similar pressure coefficients for the same vibrational modes [54]; however, the pressure coefficients of this group of compounds were not provided Literature reports no detailed data of Raman-active modes of A-type Gd_2O_3 in the few HP-RS measurements, where this phase is distinguished.

Since no RS study has been conducted in Yb-doped Gd_2O_3 and the few HP-RS studies performed in Gd_2O_3 have left many unanswered questions, we report in this work a vibrational study of $Gd_{1.78}Yb_{0.22}O_3$ at HP by means of HP-RS measurements up to 20.5 GPa complemented with lattice dynamics *ab initio* calculations for pure Gd_2O_3. Raman spectroscopy is a non-destructive technique that is optimal for understanding the changes in the structure of the sample and identify the PTs easily as it is very sensitive to the vibrations in the local structure [55]. HP-RS measurements of $(Gd_{1-x}Yb_x)_2O_3$ (x = 0.11) revealed a first PT from the C-type to the B-type phase at 6.2 GPa followed by a second PT towards the A-type phase around 9.8 GPa. As expected, we have observed on downstroke the A-B PT below 9.8 GPa (Fig. 1). Finally, we must mention that theoretical calculations have helped to identify the Raman-active modes of the different polymorphs and to assign the symmetry of the first-order Raman-active modes of each phase along the pressure range studied. Moreover, we report the experimental Raman-active modes of the three phases of $(Gd_{1-x}Yb_x)_2O_3$ (x = 0.11) as a function of pressure and the corresponding pressure coefficients, showing a nice agreement with theoretically simulated frequencies and HP dependences of pure Gd_2O_3 and Tb_2O_3. In particular, we provide for the first time the four Raman-active modes of the A-type phase of Gd_2O_3. A comparison of the pressure coefficients of the Raman-active modes of the three phases with those isostructural RE SOs is also provided.

2. Experimental details

The samples used in this study were millimeter-sized pure cubic $Gd_{1.78}Yb_{0.22}O_3$ single crystals synthesized from commercial powders of raw materials (Gd_2O_3, Yb_2O_3, Li_2CO_3 and H_3BO_3) of 4N purity that were used as received. The crystal growth of $Gd_{1.78}Yb_{0.22}O_3$ single crystals was performed by high-temperature solution growth, using a $Li_6(Gd_{0.95}Yb_{0.05})(BO_3)_3$ solvent, in several stages that differ a little bit from the processes described in [56]. At first, a solute of formula $(Gd_{0.95}Yb_{0.05})_2O_3$ was prepared by reacting together a stoichiometric

and mechanically mixed amount of Gd_2O_3 and Yb_2O_3 powders. Then, the $Li_6(Gd_{0.95}Yb_{0.05})(BO_3)_3$ solvent was synthesized by mechanically mixing and grinding stoichiometric amounts of the hereabove mentioned powders, which were subsequently heated in air in a Pt crucible at 450 °C for 12 h, and at 750 °C for 12 h. Finally, a growth load composed of 80 mol% of $Li_6(Gd_{0.95}Yb_{0.05})(BO_3)_3$ solvent and 20 mol% of solute $(Gd_{0.95}Yb_{0.05})_2O_3$ was mechanically mixed and ground together with an additional amount of Li_2CO_3 powder (equivalent to an excess of 19.35 mol.% of Li_2O). Melting of this mixture in air in a Pt crucible was performed at 1250 °C, after two successive 12 h-long heating stages at 500 °C and at 800 °C. The typical temperature gradients in the furnace was 1 °C/cm. Growth was initiated on a Pt disk immersed into the melt. The molten bath stirring was ensured by rotating the alumina rod at 30 rpm for 24 h at 1250 °C in order to dissolve completely the solute and homogenize the melt composition. The slow cooling of the flux occurred at −0.2 °C/h from 1250 °C to 1100 °C, with a saw-teeth profile optimized according to the supersaturation temperature determination. At 1100 °C, the disk was removed from the molten bath, and then the whole setup was allowed to cool down to 1000 °C at −0.5 °C/h and to room temperature at −60 °C/h. The Ia-3 space group of the cubic phase and the uniform Yb-content in the resulting crystals were confirmed by structural (Laue, powder XRD) and chemical (EPMA/WDS) characterizations of the crystals exactly in the same way as described in reference [56]. The lattice parameter of the $Gd_{1.78}Yb_{0.22}O_3$ crystal was estimated to be a = 10.749 Å. Characterizations, spectroscopic properties and laser operation of a similar sample with 14% of Yb were measured and discussed in references [57] and [3].

Room-temperature unpolarized HP-RS measurements up to 20.5 GPa were excited with the 632.8 nm line of a HeNe laser. For these experiments, 50 × 50 μm^2 pieces (around 20 μm in thickness) without known orientation were obtained from millimeter-size Tb_2O_3 single crystals. Inelastically-scattered light was collected with a Horiba Jobin Yvon LabRAM HR UV spectrometer equipped with an edge filter that cuts Raman signals below ~50 cm^{-1} and a thermoelectrically cooled multichannel CCD detector enabling a spectral resolution better than 2 cm^{-1} [58]. The samples were located in a 150-μm diameter hole performed in a 40 μm thick steel gasket in a diamond anvil cell with 400 μm diameter culet together with small ruby chips evenly distributed that allow the determination of the applied pressure [59]. A 4:1 methanol:ethanol mixture was used as a pressure-transmitting medium. Phonon signals were analyzed by fitting the Raman peaks with a pseudo-Voigt profile.

3. Theoretical *ab initio* simulation details

Ab initio total-energy calculations at 0 K for the C-, B-, and A-type phases of Gd_2O_3 were performed within the framework of density functional theory (DFT) [60] with the Vienna Ab-initio Simulation Package (VASP) [61], using the pseudopotential method and the projector augmented waves (PAW) scheme [62,63]. In this work, the generalized gradient approximation (GGA) with the Perdew–Burke–Ernzerhof parametrization for solids (PBEsol) was used for the exchange and correlation energy [64]. A dense Monkhorst–Pack grid of special k-points [65] (6 × 6 × 6 for the C phase and 4 × 4 × 4 for the A and B phases) and a plane-wave basis set with energy cutoffs of 530 eV were used. This ensures a convergence of 1 meV per formula unit for the total energy. For each phase, the lattice parameters and atomic positions at selected volumes were fully optimized through the calculation of the forces on the atoms and the stress tensor. The optimization criterion was to relax the configuration until the stress tensor deviations from the diagonal form were lower than 0.1 GPa, and the forces on the atoms smaller than 0.004 eV/Å. Through this process, the stress for each volume and so the theoretical pressure P (V) were obtained. The set of accurate results of energy (E), volume (V), and pressure (P) data, provided by calculations allow to derive the enthalpy (H) as a pressure function H(P) and so to determine the relative stability of the phase under study and the transition pressure. Lattice-dynamical properties were obtained for the Γ-point using the direct-force constant approach, at several pressures [66]. The diagonalization of the dynamical matrix, which requires separate calculations of highly converged forces, provides the frequency of the Raman and infrared modes. These calculations also allow identifying the symmetry and eigenvectors of the vibrational modes for the considered structure.

4. Results and discussion

The lattice dynamics of C-type Gd_2O_3 yields 120 normal vibrational modes at the Γ-point whose mechanical decomposition is:

$$\Gamma_{\text{cubic}} = 4A_g(R) + 4E_g(R) + 14F_g(R) + 5A_{2u}(I) + 5E_u(I) + 16F_u(IR) + 1F_u(Ac) \quad (1)$$

where A_{2u} and E_u modes are inactive (I), A_g, E_g and F_g (or T_g) modes are Raman-active (R), one F_u mode is acoustic (Ac) and the other $16F_u$ (or T_u) modes are infrared-active (IR). The E modes are doubly degenerated, and the F modes are triply degenerated. Consequently, one expects 22 Raman-active modes ($\Gamma_{Raman} = 4A_g + 4E_g + 14F_g$) and 16 IR-active modes ($16F_u$). On the other hand, the lattice dynamics of B-type Gd_2O_3 has 45 normal vibrational modes at the Γ-point whose mechanical decomposition is:

$$\Gamma_{monoclinic} = 14A_g(R) + 7B_g(R) + 7A_u(IR) + 14B_u(IR) + A_u(Ac) + 2B_u(Ac) \quad (2)$$

thus, one expects 21 Raman active modes ($\Gamma_{Raman} = 14A_g + 7B_g$) and 21 IR active modes ($\Gamma_{IR} = 14A_u + 7B_u$). Finally, the lattice dynamics of A-type Gd_2O_3 has 15 normal vibrational modes at the Γ-point whose mechanical decomposition is:

$$\Gamma_{trigonal} = 2A_{1g}(R) + 2E_g(R) + 2A_u(IR) + 2E_u(IR) + A_{2u}(Ac) + E_u(Ac) \quad (3)$$

Thus, one expects 4 Raman-active modes ($\Gamma_{Raman} = 2A_g + 2E_g$) and 4 IR-active modes ($\Gamma_{IR} = 2A_u + 2E_u$).

Fig. 2(a) and (b) show the RS spectra of the $Gd_{1.78}Yb_{0.22}O_3$ sample on upstroke (up to 20.5 GPa) and on downstroke (to room pressure), respectively. The RS spectrum of the sample at room pressure corresponds to the C-type structure and the peaks of the cubic phase are followed up to 6 GPa. Above that pressure, the main peaks of the cubic phase decrease in intensity and new peaks appear. The large number of new peaks is consistent with the less symmetric B-type structure. On further increase of pressure, the RS spectrum changes completely above 10 GPa. At this pressure, only main four modes are observed that are consistent with the A-type phase. This phase is stable up to the maximum pressure attained in our study (20.5 GPa). On downstroke from 20.5 GPa, the A-type phase remains until 9.8 GPa. Below this pressure, the B-type phase is found, and it becomes the recovered phase when pressure is fully released. Our results are supported by the theoretically simulated frequencies of the Raman-active modes in the three phases at different pressures as shown by the vertical ticks at the bottom part of selected spectra in Fig. 2.

Despite the 11% of Yb atoms substituting Gd atoms in the crystalline structure, the C-B (6 GPa) and B-A (9.8 GPa) PTs observed in $Gd_{1.78}Yb_{0.22}O_3$ match with the trends showed by these two PTs in *RE* SOs as a function of the cationic radius, as recently reviewed [67]. In this context, it must be noted that the lattice parameter of our sample (10.749 Å) leads to a unit-cell volume per formula unit of 77.62 Å^3 that is in between those for pure Gd_2O_3 and pure Tb_2O_3 [41]. Therefore, the two PT pressures in our sample, which are slightly smaller than those recently found for both PTs in Tb_2O_3

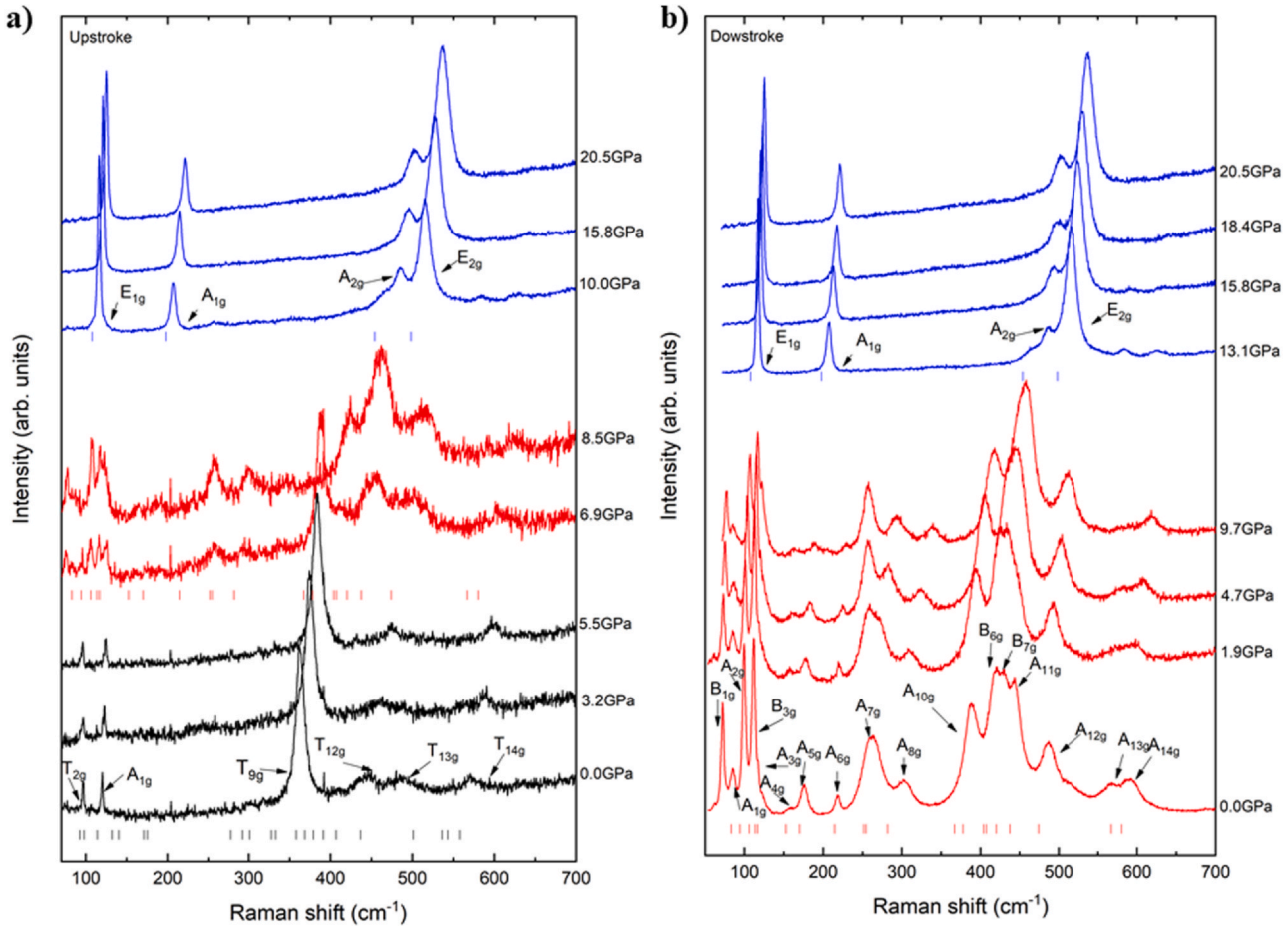

Fig. 2. Raman spectra of $Gd_{1.78}Yb_{0.22}O_3$ on upstroke (a) and downstroke (b) at selected pressures (vertically shifted for the sake of clarity). Vertical ticks indicate the *ab initio* computed frequencies of first-order Raman-active modes. Black, red and blue colors represent the cubic, monoclinic and trigonal phase, respectively.

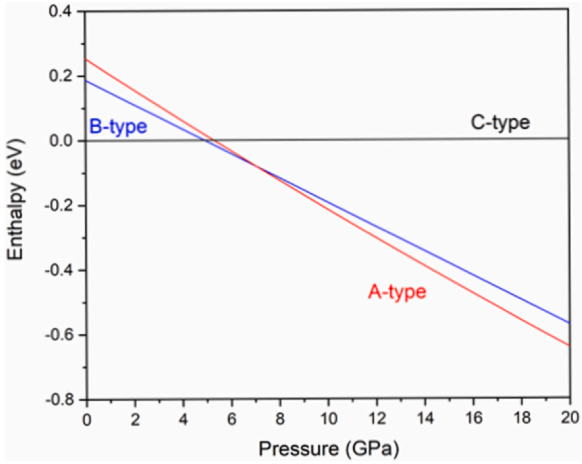

Fig. 3. Theoretical enthalpy difference of the B-type (blue line) and A-type (red line) phases of Gd_2O_3 with respect to the C-type (black line) phase as a function of pressure.

(around 7 and 12 GPa, respectively) [41] match with the expected trends. Moreover, they match with our theoretical calculations for pure Gd_2O_3 that predict a first C-B PT at 4.9 GPa, and a second B-A PT at 7.3 GPa (see Fig. 3). Note that our theoretical values for the PT pressures also agree with the theoretical values (GGA-PBE) recently published for Tb_2O_3 (5.5 and 10.9 GPa, respectively) [41].

Curiously, our PT sequence in $Gd_{1.78}Yb_{0.22}O_3$ on upstroke does not agree with those found in pure bulk and nanocrystalline Gd_2O_3, as summarized in the introduction section, since the C-A PT was the only reported PT on upstroke under static compression [44–54]. Only a B-type phase was observed on after shock-wave compression [42,43] and during pre-compression of pure Gd_2O_3 powders into a pellet at a non-hydrostatic pressure around 2.5 GPa [49]. It must be noted that most of the studies performed on Gd_2O_3 at HP used XRD techniques that are not good techniques to observe minority phases when there is a coexistence of phases. In this context, we have to note that in our measurements, the C-type phase coexisted with the B-type phase between 6 and 8.5 GPa (since the main peak of the C-type phase is observed up to this pressure). The cubic phase was also observed up to 8.5 GPa in Er-doped Gd_2O_3 [51] while it was observed well above 10 GPa and up to 15 GPa in pure Gd_2O_3 [47,49,50]. Therefore, since the A-type phase is claimed to appear above 7 GPa in pure samples, the B-type phase, if it is present in pure samples between the C and A phases, could not be found as a single phase what makes difficult its observation with HP-XRD measurements.

There are only two studies reporting HP-RS measurements on Gd_2O_3 [48,52]. Dilawar et al. performed measurements on 30-nm nanocrystals and observed a C-A PT with considerable amorphization, while Zhang et al. performed measurements on pure powder and observed a C-A PT. Notably, the quality of the RS spectra of these two works is much smaller than ours likely due to our use of single crystals instead of microcrystalline or nanocrystalline powders as used in previous studies. Therefore, we think that the lack of observation of the B-type phase in pure Gd_2O_3 as a HP phase intermediate between the C- and A-type phases could be related to the use of powders instead of single crystals, as in our present study, and/or to the fact that PL and RS measurements are more local

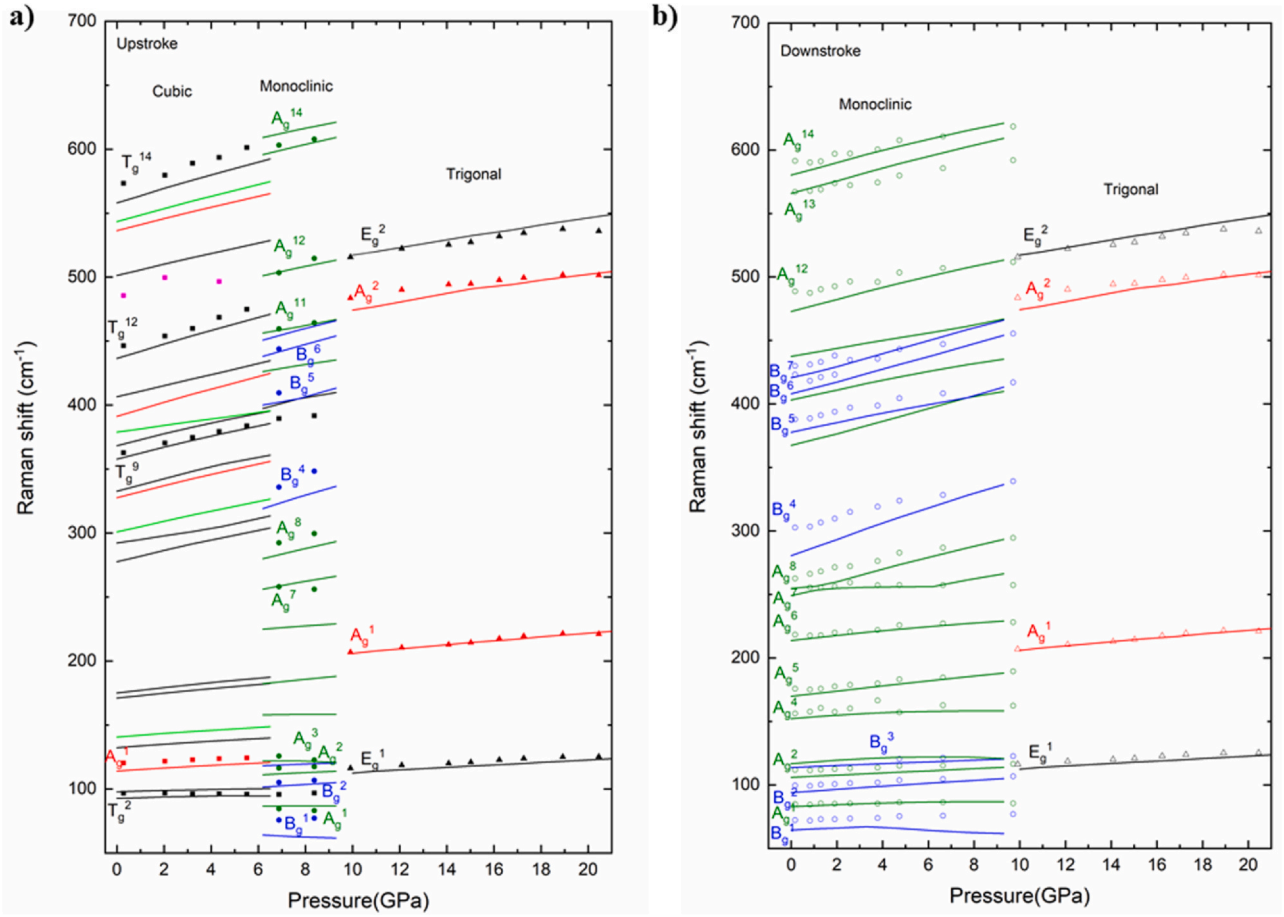

Fig. 4. Pressure dependence of experimental (theoretical) frequencies of the Raman-active modes observed in $Gd_{1.78}Yb_{0.22}O_3$ (pure Gd_2O_3) on upstroke (a) and downstroke (b) represented by symbols (lines). The tentatively assigned symmetries of the experimental modes are provided.

techniques than XRD measurements and are able to detect minor phases that are below the threshold to be detected by actual XRD measurements, as already commented. In any case, the effect of doping on Gd_2O_3 cannot be discarded and must be solved with future experiments in pure Gd_2O_3 single crystals.

Fig. 4(a) and (b) show the pressure dependence of the Raman-active modes in the three phases of $Gd_{1.78}Yb_{0.22}O_3$ both on upstroke and downstroke, respectively. On upstroke, a coexistence of C- and B-type phases is clearly seen at 7 GPa. The frequencies of the peaks in the experimental Raman spectrum and the theoretical frequencies for pure Gd_2O_3 are represented as a function of pressure in order to confirm the identification of the modes of the different phases and the assignation of the symmetry of each experimental mode. As observed, the frequencies and pressure coefficients of most Raman modes in $Gd_{1.78}Yb_{0.22}O_3$ agree with those theoretically expected for pure Gd_2O_3 in the three phases, so we have performed a tentative assignment in the light of the match between the experimental and theoretical frequencies and pressure coefficients. Tables 1–3 summarize the experimental and theoretical frequencies and pressure coefficients for the C-, B- and A-type phases, respectively, of experimental Yb-doped Gd_2O_3 and theoretical pure Gd_2O_3 when fitted to a linear relationship $\omega=\omega_0+\alpha_1 \cdot P$.

As regards the experimental frequencies of C-type $Gd_{1.78}Yb_{0.22}O_3$, it is observed that they match with those experimentally reported for pure Gd_2O_3 [13,14,17,18]. Therefore, we have not observed a deviation of the phonon frequencies of our sample due to the 11% at. Yb concentration with respect to pure Gd_2O_3. Note that a slight downward shift of some vibrational frequencies, especially in the low-frequency region below 200 cm^{-1}, would be expected due to the larger mass of Yb than Gd. We must also stress that the measured frequencies of the low-frequency Raman-active modes in C-type $Gd_{1.78}Yb_{0.22}O_3$ have slightly larger frequencies than those of C-type Tb_2O_3. This is consistent with the expected behaviour for pure Gd_2O_3 due to the smaller mass of Gd than Tb and the strong dependence of the low-frequency modes with the cation mass [18]. It must be noted that our theoretical Raman-active modes of C-type Gd_2O_3 (Table 1) show similar frequencies and pressure coefficients than those recently published for C-type Tb_2O_3 [41]. In C-type $Gd_{1.78}Yb_{0.22}O_3$ single crystal, 5 modes out of 22 theoretically predicted were followed under pressure, unlike in Tb_2O_3 single crystal where 10 modes were observed. A broad band located at 488 cm^{-1} at room pressure and with a pressure coefficient of 2.5 cm^{-1}/GPa is the only observed mode that does not match with the expected values of frequency and pressure coefficient of the first-order Raman-active modes in pure Gd_2O_3 (see Table 1). We can speculate that this mode could correspond to a second-order Raman mode or to a local mode due to Yb doping.

A comparison of the experimental frequencies and pressure coefficients of C-type $Gd_{1.78}Yb_{0.22}O_3$ and the experimental and theoretical data for pure Gd_2O_3 shows a nice agreement with the symmetry assignment provided by Abrasev et al. for the observed modes. We have not observed the mode at 315 cm^{-1} that was attributed to a E_g+F_g mode [18]; however, our calculations, that tend to slightly underestimate the experimental frequencies, as it was also found in Tb_2O_3 [41], suggest that this mode must be the E_g^2 mode (see Table 1) since the frequencies of the nearest calculated F_g (or T_g) modes are either at much lower or at higher frequencies than the experimental one. Regarding the pressure coefficients of the Raman-

Table 1
Theoretical (the.) and experimental (exp.) zero-pressure frequencies, ω_0 (in cm^{-1}), and linear pressure coefficients, α_1 (in cm^{-1}/GPa), of the Raman-active modes in the cubic phase of Gd_2O_3, $Gd_{1.78}Yb_{0.22}O_3$ and Tb_2O_3.

Symmetry	Gd_2O_3 (the.)		Gd_2O_3 (exp.)		$Gd_{1.78}Yb_{0.22}O_3$ (exp.)		Tb_2O_3 (the.)[c]		Tb_2O_3 (exp.)[c]	
	ω_0	α_1	ω_0[a]	α_1[b]	ω_0	α_1	ω_0	α_1	ω_0	α_1
T_g^1	92.7	0.4	95[a]		96.8(2)	0.2(5)	95.1	-0.1	94.5	-0.3
T_g^2	97.9	0.4	110[a]				98.4	0.4	106.2	-0.2
A_g^1	114.0	1.1	119[a]		120.0(2)	0.8(5)	114.3	1.0	118.6	0.7
T_g^3	132.3	1.3	135[a]				132.4	0.1	134.2	0.9
E_g^1	140.5	1.3	145[a]				143.1	0.9	144.4	0.8
T_g^4	171.1	1.6	175[a]				171.4	1.7		
T_g^5	175.1	2.0					177.5	1.5		
T_g^6	277.7	4.2					295.3	2.6		
T_g^7	292.2	2.9					300.7	2.6		
E_g^2	300.9	3.8	315[a],317[b]	3.6			311.1	3.3	320.0	2.9
T_g^8	327.6	4.7					330.6	4.3		
A_g^2	332.8	4.5					345.0	2.3		
T_g^9	357.8	4.5	361[a],363[b]	4.1	361.8(2)	4.0(6)	360.7	4.3	366.7	3.9
E_g^3	368.3	2.6					365.1	4.7		
T_g^{10}	378.8	4.4					372.7	4.1		
A_g^3	391.3	4.9	401[b]	3.2			396.8	5.1	404.7	4.33
T_g^{11}	406.6	4.4	414[a]				411.1	4.4		
T_g^{12}	436.6	5.1	444[a],445[b]	5.3	443.2(1)	5.6(4)	442.1	5.3	452.4	4.8
T_g^{13}	501.3	4.1	495[b]	3.4	488.1(7)	2.5(2)[d]	505.2	4.3		
A_g^4	536.4	4.3					541.5	4.5		
E_g^4	543.5	4.6					548.4	4.8		
T_g^{14}	558.0	5.0	569[a,b]		571.2(1)	5.4(4)	563.5	5.3	576.4	4.8

[a] Ref. [18].
[b] Obtained from Ref. [48] (Gd_2O_3-30 nm nanocrystals).
[c] Tb_2O_3 data from Ref. [41].
[d] This band is likely a second-order mode or a mode related to Yb since neither the frequency nor the pressure coefficient match with theoretical calculations nor with that observed in Tb_2O_3.

active modes, they tend to increase with the frequency, as already noted for Tb_2O_3 [41]. It must be noted that the Raman-active mode of 443 cm^{-1} has the largest pressure coefficient in good agreement with the results found in pure Gd_2O_3 nanocrystals [48].

As regards the experimental frequencies of B-type $Gd_{1.78}Yb_{0.22}O_3$, it is observed that they match with those experimentally reported for pure Gd_2O_3 [9,10,12,19]. Again, we have not observed a deviation of the phonon frequencies of our B-type sample due to the 11% at. Yb concentration with respect to pure Gd_2O_3. As already commented, a slight downward shift of some frequencies, especially at the low-frequency region below 200 cm^{-1}, would be expected due to the larger mass of Yb than Gd. We must note that the measured frequencies of the low-frequency Raman-active modes in B-type $Gd_{1.78}Yb_{0.22}O_3$ have slightly larger frequencies than those of B-type Tb_2O_3. This is consistent with the expected behaviour for pure Gd_2O_3 due to the smaller mass of Gd than Tb and the strong dependence of the low-frequency modes with the cation mass [10]. All experimentally Raman-active modes of B-type $Gd_{1.78}Yb_{0.22}O_3$ have been attributed to Raman modes corresponding to pure Gd_2O_3 (see Table 2). A comparison of the experimental frequencies of B-type $Gd_{1.78}Yb_{0.22}O_3$ and the experimental and theoretical data for pure Gd_2O_3 shows a nice agreement with the symmetry assignment provided by Zarembowitch et al. and Gouteron

Table 2
Theoretical (the.) and experimental (exp.) zero-pressure frequencies, ω_0 (in cm^{-1}), and linear pressure coefficients, α_1 (in cm^{-1}/GPa), of the Raman-active modes in the monoclinic phase of Gd_2O_3, $Gd_{1.78}Yb_{0.22}O_3$ and Tb_2O_3.

Symmetry	Gd_2O_3 (the.)		Gd_2O_3 (exp.)[a]	$Gd_{1.78}Yb_{0.22}O_3$ (exp.)		Tb_2O_3 (the.)[b]		Tb_2O_3 (exp.)[b]	
	ω_0	α_1	ω_0	ω_0	α_1	ω_0	α_1	ω_0	α_1
B_g^1	64.4	0.8	71	72(1)	0.5(4)	64.6	0.7	70.3	0.7
A_g^1	82.9	0.7	84	85(2)	0.5(2)	82.9	0.4	82.9	0.01
B_g^2	94.1	1.2	98	99(2)	0.8(4)	94.1	1.2	96.8	1.2
A_g^2	106.0	0.9	109	111.5(2)	0.6(5)	106.6	0.8	110.8	0.6
B_g^3	113.8	0.7	115	118.4(7)[d]	0.4(9)	113.6	0.7		
A_g^3	116.8	1.2	123			117.4	0.4	122.9	0.1
A_g^4	152.6	1.1	150	157.0(1)	0.9(7)	152.9	0.6	156.3	0.9
A_g^5	170.1	1.9	176	174.5(4)	1.6(9)	169.6	1.9	172.8	2.1
A_g^6	214.5	1.6	218	217.5(7)	1.3(1)	213.5	1.6	216.5	1.8
A_g^7	251.6	0.3	256	254.9(3)	0.8(1)	251.0	0.5	261.8	-0.23
A_g^8	254.6	4.3	269	263.9(8)	3.4(2)	258.5	4.1	265.2	5.1
B_g^4	281.9	5.8	299	302.0(1)	3.9(2)	282.9	5.8	306.6	5.1
A_g^9	367.1	4.8	385			371.1	4.7	368.6	1.7
B_g^5	378.0	3.6	387	387.5(7)	3.1(1)	381.5	3.3		
A_g^{10}	403.9	3.5				408.2	3.3	391.7	3.8
B_g^6	407.2	5.1	416	419.0(2)	4.0(5)	411.3	4.9		
B_g^7	420.4	4.8	427	428.0(1)	5.0(6)	424.2	4.5	426.2	2.4
A_g^{11}	437.4	3.1	442			442.6	3.0	446.0	3.0
A_g^{12}	474.4	4.1	483	488.0(1)	2.7(2)	477.9	4.1	492.0	3.6
A_g^{13}	566.9	4.5	580	566.1(8)	2.7(2)	570.3	4.5		
A_g^{14}	580.2	4.1	590	590.0(1)	3.1(2)	585.4	4.2	596.7	3.9

[a] Refs. [9,10]. [b] Ref. [41]. [d] This mode is only observed at high pressure.

Table 3
Theoretical (the.) and experimental (exp.) frequencies, ω_0 (in cm^{-1}), and linear pressure coefficients, α_1 (in cm^{-1}/GPa), of the Raman-active modes of the trigonal phase of Gd_2O_3, $Gd_{1.78}Yb_{0.22}O_3$, and Tb_2O_3 at 11 GPa.

Symmetry	Gd_2O_3 (the.) (11 GPa)		$Gd_{1.78}Yb_{0.22}O_3$ (exp.) (11 GPa)		Tb_2O_3 (the.)[a] (11 GPa)		Tb_2O_3 (exp.)[a] (11 GPa)	
	ω_0	α_1	ω_0	α_1	ω_0	α_1	ω_0	α_1
E_g^1	120	1.0	125(1)	0.9(9)	113.7	1.0	116.0	1.4
A_g^1	220	1.6	220(2)	1.5(2)	206.6	1.5	207.7	2.1
A_g^2	485	2.9	490(3)	1.7(2)	486.6	2.3	490.3	2.3
E_g^2	525	3.0	525(3)	2.1(3)	524.7	2.9	529.2	2.8

[a] Ref. [41].

et al. for the observed modes [9,10], with the exception of the modes at 385 and 387 cm^{-1}, that we have tentatively attributed to the A_g^9 and B_g^5 modes, respectively, according to the similitude with the calculated frequencies that tend to underestimate the experimental values, as already commented. Unfortunately, we have not measured the 385 cm^{-1} mode to confirm the proposed assignment. Regarding the pressure coefficients of the Raman-active modes of the B-type phase, they tend to increase with the frequency, as already noted for B-type Tb_2O_3 [41]. As in B-type Tb_2O_3, the theoretical Raman-active mode with the highest pressure coefficient in B-type $Gd_{1.78}Yb_{0.22}O_3$ is the B_g^4 mode. It must be noted that the theoretical Raman-active modes of B-type Gd_2O_3 show similar frequencies and pressure coefficients than those recently published for B-type Tb_2O_3 [41]. In both B-type Gd_2O_3 and Tb_2O_3 16 modes out of 21 theoretically predicted were followed under pressure; however, in $Gd_{1.78}Yb_{0.22}O_3$ we measured the high-frequency A_g^{13} and B_g^6 modes that were not measured in Tb_2O_3 [41].

Finally, regarding the experimental frequencies of A-type $Gd_{1.78}Yb_{0.22}O_3$, they are reported for the first time to our knowledge so no comparison with pure Gd_2O_3 can be made. A notable agreement is found with the theoretical values expected for pure Gd_2O_3 (Table 3). Again, the calculated and measured frequencies of the low-frequency modes in A-type pure Gd_2O_3 and $Gd_{1.78}Yb_{0.22}O_3$ have larger frequencies than those calculated and measured for A-type Tb_2O_3 at a similar pressure due to the smaller mass of Gd than Tb. This behaviour shows that cation mass has a strong influence on the low-frequency modes, as already commented in a previous work [41]. In fact, if we compare the values of A-type $Gd_{1.78}Yb_{0.22}O_3$, Gd_2O_3, Sm_2O_3 and Tb_2O_3 extrapolated to room pressure with those already observed for Nd_2O_3 and La_2O_3 at room pressure (Table 4), we see that our values for Gd_2O_3 and $Gd_{1.78}Yb_{0.22}O_3$ fall between those of Tb_2O_3 and those of Sm_2O_3, as expected by the atomic mass and f electron number. Note that the values of the two low-frequency modes are similar for all *RE* SOs due to their similar atomic masses, while the values of the two high-frequency modes are quite different and increase with the f electron number in *RE* SOs.

As regards the pressure coefficients of the Raman-active modes of A-type $Gd_{1.78}Yb_{0.22}O_3$, they match with those predicted for Gd_2O_3 and with reported values for Tb_2O_3, as well as for Sm_2O_3, Nd_2O_3 and La_2O_3 (see Ref. [41]). In general, the pressure coefficients of A-type *RE* sesquioxides increase with the frequency as in C- and B-type *RE* SOs, being the lowest frequency mode around 1 cm^{-1}/GPa and the highest frequency mode around 3 cm^{-1}/GPa. As in our recent study of Tb_2O_3 [41], our present study on Gd_2O_3 confirms the strong cation influence in the two low-frequency modes of A-type *RE* SOs.

5. Conclusions

We have reported a lattice dynamics study of a single crystal of $Gd_{1.78}Yb_{0.22}O_3$ under compression up to 20.5 GPa. We have identified two phase transitions on the upstroke and one on the downstroke. On the upstroke, the cubic phase undergoes a transition to the monoclinic phase at 6.2 GPa, with coexistence of both phases up to 8.5 GPa, and the B-type phase undergoes a transition to the trigonal phase above 9.8 GPa. On the downstroke, the transition back to the monoclinic phase is observed below 9.8 GPa and the monoclinic phase is recovered in a metastable form at room pressure. This phase transition sequence is similar and with similar pressures to those recently reported for the neighbour Tb_2O_3. While the sequence of phase transitions on downstroke agrees with those previously reported in Gd_2O_3, our sequence of phase transitions on upstroke do not agree with those previously published in Gd_2O_3 that do not find evidence of the intermediate monoclinic phase. Therefore, our work opens the door for future experiments in order to verify if the disagreement is either related to Yb substitution for Gd atoms, to the use of single crystals instead of microcrystalline and nanocrystalline powders, or to the use of a more local and sensitive technique to minority phases, such as Raman scattering compared to X-ray diffraction. It must be stressed that the different phase transitions here reported have been supported by our *ab initio* lattice dynamics theoretical calculations on pure Gd_2O_3. Moreover, thanks to our calculations we have assigned all the experimentally observed Raman-active modes in the three phases of $Gd_{1.78}Yb_{0.22}O_3$ and discussed their frequencies and pressure coefficients in relation to isostructural rare-earth sesquioxides. In particular, the Raman-active modes for the trigonal A-type phase of Gd_2O_3 have been reported for the first time and nicely compared to other isostructural rare-earth sesquioxides.

CRediT authorship contribution statement

Julia Marí-Guaita: Writing - original draft, Experimental study, Characterization, Summarization, Revision. **S. Gallego-Parra:** Experimental works, Revision. **J. A. Sans:** Writing - original draft, Supervision. **M. Velázquez:** Experimental work. **Phillippe Veber:** Experimental work. **P. Rodríguez-Hernández:** Theoretical calculations. **A. Muñoz:** Theoretical calculations. **F. J. Manjón:** Writing - original draft, Visualitzation, Investigation, Supervision.

Table 4
Theoretical (the.) and experimental (exp.) frequencies, ω_0 (cm^{-1}), of the Raman-active modes of the trigonal-A phase of Gd_2O_3, $Gd_{1.78}Yb_{0.22}O_3$,Tb_2O_3, Sm_2O_3, Nd_2O_3, and La_2O_3 at 0 GPa.

Symmetry	La_2O_3 (exp.)[a]	Nd_2O_3 (exp.)[b]	Sm_2O_3 (exp.)[c]	Gd_2O_3 (the.)[d]	$Gd_{1.78}Yb_{0.22}O_3$ (exp.)[d]	Tb_2O_3 (the.)[e]	Tb_2O_3 (exp.)[e]
	ω_0	ω_0	ω_0	ω_0	ω_0	ω_0	ω_0
E_g^1	106	107	105	107.7	106.1(1)	113.7	116.0
A_g^1	191	193	188	197.7	191.0(3)	206.6	207.7
A_g^2	400	427	444	454.1	469.2(3)	486.6	490.3
E_g^2	408	437	455	498.3	494.3(5)	524.7	529.2

[a] Ref. [68].
[b] Ref. [69].
[c] Ref. [10]
[d] Estimated from this work.
[e] Estimated from Ref. [41].

Declaration of Competing Interest

The authors declare that they have no known competing financial interests or personal relationships that could have appeared to influence the work reported in this paper.

Acknowledgements

This work was supported by the Generalitat Valenciana under Project PROMETEO 2018/123-EFIMAT and by the Spanish Ministerio de Ciencia e Innovación and Agencia Estatal de Investigación under Projects MAT2016–75586-C4–2-P/3-P, FIS2017-83295-P, and PID2019–106383GB-42/43, as well as through MALTA Consolider Team Research Network (RED2018–102612-T). A. Muñoz and P. Rodríguez-Hernández acknowledge computing time provided by Red Española de Supercomputación (RES) and the MALTA Consolider Team cluster. J.A. Sans acknowledge Ramón y Cajal Fellowship (RYC-2015–17482) for funding support.

References

[1] G.Y. Adachi, N. Imanaka, The binary rare earth oxides, Chem. Rev. 98 (1998) 1479–1514, https://doi.org/10.1021/cr940055h
[2] M. Hong, J. Kwo, A.R. Kortan, J.P. Mannaerts, A.M. Sergent, Epitaxial cubic gadolinium oxide as a dielectric for gallium arsenide passivation, Science 283 (1999) 1897–1900, https://doi.org/10.1126/science.283.5409.1897
[3] F. Druon, M. Velázquez, P. Veber, S. Janicot, O. Viraphong, G. Buşe, M.A. Ahmed, T. Graf, D. Rytz, P. Georges, Laser demonstration with highly doped Yb:Gd_2O_3 and Yb:Y_2O_3 crystals grown by an original flux method, Opt. Lett. 38 (2013) 4146, https://doi.org/10.1364/ol.38.004146
[4] J. Križan, M. Mazaj, V. Kaučič, I. Bajsić, J. Možina, Synthesis of Er- and Yb-doped gadolinium oxide polymorphs and influence of their structures on upconversion properties, Acta Chim. Slov. 61 (2014) 608–614.
[5] R.K. Tamrakar, D.P. Bisen, Thermoluminescence studies of ultraviolet and gamma irradiated erbium(III)- and ytterbium(III)-doped gadolinium oxide phosphors, Mater. Sci. Semicond. Process. 33 (2015) 169–188, https://doi.org/10.1016/j.mssp.2015.01.044
[6] V.A. Pustovarov, E.S. Trofimova, Y.A. Kuznetsova, A.F. Zatsepin, Upconversion luminescence of Gd_2O_3 nanocrystals doped with Er^{3+} and Yb^{3+} ions, Tech. Phys. Lett. 44 (2018) 622–625, https://doi.org/10.1134/S106378501807026X
[7] I. Warshaw, R. Roy, Polymorphism of the rare earth sesquioxides, J. Phys. Chem. 65 (1961) 2048–2051, https://doi.org/10.1021/j100828a030
[8] H.R. Hoekstra, Phase relationships in the rare earth sesquioxides at high pressure, Inorg. Chem. 5 (1966) 754–757, https://doi.org/10.1021/ic50039a013
[9] J. Zarembowitch, J. Gouteron, A.M. Lejus, Raman spectrum of single crystals of monoclinic B-type gadolinium sesquioxide, J. Raman Spectrosc. 9 (1980) 263–265, https://doi.org/10.1002/jrs.1250090410
[10] J. Gouteron, D. Michel, Raman spectra of lanthanide sesquioxide single correlation between A and B-Type structures crystals, J. Solid. State Chem. 38 (1981) 288–296, https://doi.org/10.1016/0022-4596(81)90058-X
[11] M.W. Urban, B.C. Cornilsen, Bonding anomalies in the rare earth sesquioxides, J. Phys. Chem. 48 (1987) 475–479, https://doi.org/10.1016/0022-3697(87)90108-9
[12] L. Laversenne, Y. Guyot, C. Goutaudier, M.T. Cohen-Adad, G. Boulon, Optimization of spectroscopic properties of Yb^{3+}-doped refractory sesquioxides: Cubic Y_2O_3, Lu_2O_3 and monoclinic Gd_2O_3, Opt. Mater. (Amst.). 16 (2001) 475–483, https://doi.org/10.1016/S0925-3467(00)00095-1
[13] C. Le Luyer, A. García-Murillo, E. Bernstein, J. Mugnier, Waveguide Raman spectroscopy of sol-gel Gd_2O_3 thin films, J. Raman Spectrosc. 34 (2003) 234–239, https://doi.org/10.1002/jrs.980
[14] N. Dilawar, S. Mehrotra, D. Varandani, B.V. Kumaraswamy, S.K. Haldar, A.K. Bandyopadhyay, A Raman spectroscopic study of C-type rare earth sesquioxides, Mater. Charact. 59 (2008) 462–467, https://doi.org/10.1016/j.matchar.2007.04.008
[15] A. Ubaldini, M. Maddalena, Raman characterisation of powder of cubic RE_2O_3(RE = Nd, Gd, Dy, Tm, and Lu), Sc_2O_3 and Y_2O_3, J. Alloy. Compd. 454 (2008) 374–378, https://doi.org/10.1016/j.jallcom.2006.12.067
[16] P. Mele, C. Artini, A. Ubaldini, G.A. Costa, M.M. Carnasciali, R. Masini, Synthesis, structure and magnetic properties in the Nd_2O_3-Gd_2O_3 mixed system synthesized at 1200 °C, J. Phys. Chem. Solids 70 (2009) 276–280, https://doi.org/10.1016/j.jpcs.2008.10.010
[17] J. Yu, L. Cui, H. He, S. Yan, Y. Hu, H. Wu, Raman spectra of RE_2O_3 (RE=Eu, Gd, Dy, Ho, Er, Tm, Yb, Lu, Sc and Y): Laser-excited luminescence and trace impurity analysis, J. Rare Earths 32 (2014) 1–4, https://doi.org/10.1016/S1002-0721(14)60025-9
[18] M.V. Abrashev, N.D. Todorov, J. Geshev, Raman spectra of R_2O_3 (R – Rare earth) sesquioxides with C-type bixbyite crystal structure: a comparative study, J. Appl. Phys. 116 (2014) 103508, https://doi.org/10.1063/1.4894775
[19] Y.T. Foo, A.Z. Abdullah, B. Amini Horri, B. Salamatinia, Ammonium oxalate-assisted synthesis of Gd_2O_3 nanopowders, Ceram. Int. 45 (2019) 9082–9091, https://doi.org/10.1016/j.ceramint.2019.01.245
[20] Y.N. Xu, Z.Q. Gu, W.Y. Ching, Electronic, structural, and optical properties of crystalline yttria, Phys. Rev. B 56 (1997) 993–1000, https://doi.org/10.1103/PhysRevB.56.14993
[21] N. Hirosaki, S. Ogata, C. Kocer, Ab initio calculation of the crystal structure of the lanthanide Ln_2O_3 sesquioxides, J. Alloy. Compd. 351 (2003) 31–34, https://doi.org/10.1016/S0925-8388(02)01043-5
[22] L. Marsella, V. Fiorentini, Structure and stability of rare-earth and transition-metal oxides, Phys. Rev. B 69 (2004) 2–5, https://doi.org/10.1103/PhysRevB.69.172103
[23] L. Petit, A. Svane, Z. Szotek, W.M. Temmerman, O. Ce, First-principles study of rare-earth oxides, Phys. Rev. B 72 (2005) 1–9, https://doi.org/10.1103/PhysRevB.72.205118
[24] W.U. Bo, M. Zinkevich, W. Chong, F. Aldinger, Ab initio energetic study of oxide ceramics with rare-earth elements, Rare Metals 25 (2006) 549–555, https://doi.org/10.1016/S1001-0521(06)60097-1
[25] N. Singh, S.M. Saini, T. Nautiyal, S. Auluck, Electronic structure and optical properties of rare earth sesquioxides (R_2O_3, R=La, Pr, and Nd), J. Appl. Phys. 100 (2006) 083525, https://doi.org/10.1063/1.2353267
[26] M. Mikami, S. Nakamura, Electronic structure of rare-earth sesquioxides and oxysulfides, J. Alloy. Compd. 408–412 (2006) 687–692, https://doi.org/10.1016/j.jallcom.2005.01.068
[27] B. Wu, M. Zinkevich, F. Aldinger, D. Wen, L. Chen, Ab initio study on structure and phase transition of A - and B -type rare-earth sesquioxides Ln_2O_3 (Ln¼La – Lu, Y, and Sc) based on density function theory, J. Solid State Chem. 180 (2007) 3280–3287, https://doi.org/10.1016/j.jssc.2007.09.022
[28] M. Rahm, N.V. Skorodumova, Phase stability of the rare-earth sesquioxides under pressure, Phys. Rev. B 80 (2009) 1–7, https://doi.org/10.1103/PhysRevB.80.104105
[29] H. Jiang, R.I. Gomez-Abal, P. Rinke, M. Scheffler, Localized and itinerant states in lanthanide oxides united by GW@LDA+U, Phys. Rev. Lett. 102 (2009) 1–4, https://doi.org/10.1103/PhysRevLett.102.126403
[30] P.P. Bose, M.K. Gupta, R. Mittal, S. Rols, S.N. Achary, A.K. Tyagi, S.L. Chaplot, Phase transitions and thermodynamic properties of yttria, Y_2O_3: inelastic neutron scattering shell model and first-principles calculations, Phys. Rev. B 84 (2011) 1–11, https://doi.org/10.1103/PhysRevB.84.094301
[31] R. Gillen, S.J. Clark, J. Robertson, Nature of the electronic band gap in lanthanide oxides, Phys. Rev. B 87 (2013) 1–6, https://doi.org/10.1103/PhysRevB.87.125116
[32] D. Richard, E.L. Mu, Ab initio LSDA and LSDA + U study of pure and Cd-doped cubic lanthanide sesquioxides, Phys. Rev. B 88 (2013) 1–13, https://doi.org/10.1103/PhysRevB.88.165206
[33] H.A. Badehian, H. Salehi, M. Ghoohestani, First-principles study of elastic, structural, electronic, thermodynamical, and optical properties of Yttria (Y_2O_3) ceramic in cubic phase, J. Am. Ceram. Soc. 96 (2013) 1832–1840, https://doi.org/10.1111/jace.12259
[34] D. Richard, L.A. Errico, M. Rentería, Structural properties and the pressure-induced C → A phase transition of lanthanide sesquioxides from DFT and DFT + U calculations, J. Alloy. Compd. 664 (2016) 580–589, https://doi.org/10.1016/j.jallcom.2015.12.236
[35] X. Zhang, W. Gui, Q. Zeng, First-principles study of structural, mechanical, and thermodynamic properties of cubic Y_2O_3 under high pressure, Ceram. Int. 43 (2017) 3346–3355, https://doi.org/10.1016/j.ceramint.2016.11.176
[36] T. Ogawa, N. Otani, T. Yokoi, C.A.J. Fisher, A. Kuwabara, H. Moriwake, M. Yoshiya, S. Kitaoka, M. Takata, Density functional study of the phase stability and Raman spectra of Yb2O3, Yb2SiO5 and $Yb_2Si_2O_7$ under pressure, Phys. Chem. Chem. Phys. 20 (2018) 16518–16527, https://doi.org/10.1039/c8cp02497a
[37] A.K. Pathak, T. Vazhappilly, Ab Initio study on structure, elastic, and mechanical properties of lanthanide sesquioxides, Phys. Status Solidi Basic Res. 255 (2018) 1–7, https://doi.org/10.1002/pssb.201700668
[38] D. Li, X. Zhang, C. Liu, F. Wang, H. Zhang, M. Tian, Insight into the pressure effect on the structural stability and physical properties of cubic sesquioxides X_2O_3 (X= Sc, Y and In), Vacuum 168 (2019) 108855, https://doi.org/10.1016/j.vacuum.2019.108855
[39] A.N. Kislov, A.F. Zatsepin, Yb-doping effect on structure and lattice dynamics of Gd_2O_3, J. Phys.: Condens. Matter 31 (2019) 385402, https://doi.org/10.1088/1361-648X/ab2689
[40] A.N. Kislov, A.F. Zatsepin, Defect structure and vibrational states in Eu-doped cubic gadolinium oxide, Phys. Chem. Chem. Phys. 22 (2020) 24498–24505, https://doi.org/10.1039/d0cp04281a
[41] J. Ibáñez, J.Á. Sans, V. Cuenca-Gotor, R. Oliva, Ó. Gomis, P. Rodríguez-Hernández, A. Muñoz, U. Rodríguez-Mendoza, M. Velázquez, P. Veber, C. Popescu, F.J. Manjón, Structural and lattice-dynamical properties of Tb_2O_3 under Compression: a comparative study with rare earth and related sesquioxides, Inorg. Chem. 59 (2020) 9648–9666, https://doi.org/10.1021/acs.inorgchem.0c00834
[42] T. Atou, K. Kusaba, Shock-induced phase transition of M_2O_3 (M = SC, Y, Sm, Gd, and In)-type compunds, J. Solid State Chem. 384 (1990) 378–384, https://doi.org/10.1016/0022-4596(90)90280-B
[43] T. Atou, K. Kusaba, Y. Syono, T. Kikegawa, H. Iwasaki, Pressure-induced phase transition in rare earth sesquioxides, Geophys. Monogr. Ser. 67 (1992) 469–475, https://doi.org/10.1029/GM067p0469
[44] H. Chen, C. He, L. Gong, Z. Xin-yu, B. Pattanasiri, Y.W. Li, Structural transition of Gd_2O_3:Eu induced by high pressure, Chin. Phys. Lett. 24 (2007) 158–160, https://doi.org/10.1088/0256-307X/24/1/043
[45] H. Chen, C. He, C. Gao, Y. Ma, J. Zhang, X. Wang, S. Gao, D. Li, S. Kan, G. Zou, The structural transition of Gd_2O_3 nanoparticles induced by high pressure, J. Phys.: Condens. Matter 19 (2007) 425229, https://doi.org/10.1088/0953-8984/19/42/425229

[46] D. Lonappan, N.V.C. Shekar, P.C. Sahu, B.V. Kumarasamy, A.K. Bandyopadhyay, M. Rajagopalan, Cubic to hexagonal structural transformation in Gd_2O_3 at high pressure, Philos. Mag. Lett. 88 (2008) 473–479, https://doi.org/10.1080/09500830802232534
[47] F.X. Zhang, M. Lang, J.W. Wang, U. Becker, R.C. Ewing, Structural phase transitions of cubic Gd_2O_3 at high pressures, Phys. Rev. B 78 (2008) 1–9, https://doi.org/10.1103/PhysRevB.78.064114
[48] N. Dilawar, D. Varandani, S. Mehrotra, H.K. Poswal, S.M. Sharma, Anomalous high pressure behaviour in nanosized rare earth sesquioxides, Nanotechnology 19 (2008) 115703, https://doi.org/10.1088/0957-4484/19/11/115703
[49] L. Bai, J. Liu, X. Li, S. Jiang, W. Xiao, Y. Li, L. Tang, Y. Zhang, L. Bai, J. Liu, X. Li, S. Jiang, W. Xiao, Y. Li, Pressure-induced phase transformations in cubic Gd2O3, J. Appl. Phys. 106 (2009) 073507, https://doi.org/10.1063/1.3236580
[50] J.P. Mcclure, High pressure phase transitions in the lanthanide sesquioxides, UNLV Theses, 2009, 1–154. ⟨http://digitalcommons.library.unlv.edu/theses-dissertations/137⟩.
[51] X. Zou, C. Gong, B. Liu, Q. Li, Z. Li, B. Liu, R. Liu, J. Liu, Z. Chen, B. Zou, T. Cui, X. Bai, H. Song, X-ray diffraction of cubic Gd_2O_3/Er under high pressure, Phys. Stat. Sol. B 248 (2011) 1123–1127, https://doi.org/10.1002/pssb.201000706
[52] C.C. Zhang, Z.M. Zhang, R.C. Dai, Z.P. Wang, Z.J. Ding, High pressure luminescence and raman studies on the phase transition of Gd_2O_3: Eu^{3+} nanorods, Nanosci. Nanotechnol. 11 (2011) 9887–9891, https://doi.org/10.1166/jnn.2011.5228
[53] X. Yang, Q. Li, Z. Liu, X. Bai, H. Song, M. Yao, B. Liu, R. Liu, Pressure-induced amorphization in Gd_2O_3 /Er^{3+} Nanorods, J. Phys. Chem. C 117 (2013) 8503–8508, https://doi.org/10.1021/jp312705u
[54] N.D. Sharma, J. Singh, A. Vijay, K. Samanta, S. Dogra, A.K. Bandyopadhyay, Pressure-induced structural transition trends in nanocrystalline rare-earth sesquioxides: a raman investigation, J. Phys. Chem. 120 (2016) 11679–11689, https://doi.org/10.1021/acs.jpcc.6b02104
[55] A.L.J. Pereira, J.A. Sans, R. Vilaplana, O. Gomis, F.J. Manjón, P. Rodríguez-Hernández, A. Muñoz, C. Popescu, A. Beltrán, Isostructural second-order phase transition of β-Bi_2O_3 at high pressures: an experimental and theoretical study, J. Phys. Chem. C 118 (2014) 23189–23201, https://doi.org/10.1021/jp507826j
[56] P. Veber, M. Velázquez, V. Jubera, S. Péchev, O. Viraphong, Flux growth of Yb^{3+}-doped RE_2O_3 (RE = Y,Lu) single crystals at half their melting point temperature, CrystEngComm 13 (2011) 5220–5225, https://doi.org/10.1039/c1ce00015b
[57] M. Velázquez, P. Veber, G. Buşe, Y. Petit, P. Goldner, V. Jubera, D. Rytz, A. Jaffres, M. Peltz, V. Wesemann, P. Aschehough, G. Aka, Spectroscopic properties of newly flux grown and highly Yb^{3+}-doped cubic RE_2O_3 (RE = Y, Gd, Lu) laser crystals, Opt. Mater. 39 (2015) 258–264, https://doi.org/10.1016/j.optmat.2014.11.037
[58] A.L.J. Pereira, O. Gomis, J.A. Sans, J. Pellicer-Porres, F.J. Manjón, A. Beltran, P. Rodríguez-Hernández, A. Muñoz, Pressure effects on the vibrational properties of α-Bi2O3: an experimental and theoretical study, J. Phys.: Condens. Matter 26 (2014) 225401.
[59] H.K. Mao, J. Xu, Calibration of the Ruby pressure gauge to 800 kbar under quasi-hydrostatic conditions, J. Geophys. Res. 91 (1986) 4673–4676, https://doi.org/10.1029/JB091iB05p04673
[60] P. Hohenberg, W. Kohn, Inhomogeneous electron gas, Phys. Rev. B 136 (1964) 864–871, https://doi.org/10.1103/PhysRev.136.B864
[61] G. Kresse, J. Furthmüller, Efficiency of ab-initio total energy calculations for metals and semiconductors using a plane-wave basis set, Comput. Mater. Sci. 6 (1996) 15–50, https://doi.org/10.1016/0927-0256(96)00008-0
[62] P.E. Blöchl, Projector augmented-wave method, Phys. Rev. B 50 (1994) 17953–17979, https://doi.org/10.1103/PhysRevB.50.17953
[63] D. Joubert, From ultrasoft pseudopotentials to the projector augmented-wave method, Phys. Rev. B 59 (1999) 1758–1775, https://doi.org/10.1103/PhysRevB.59.1758
[64] J.P. Perdew, A. Ruzsinszky, G.I. Csonka, O.A. Vydrov, G.E. Scuseria, L.A. Constantin, X. Zhou, K. Burke, Restoring the density-gradient expansion for exchange in solids and surfaces, Phys. Rev. Lett. 100 (2008) 1–4, https://doi.org/10.1103/PhysRevLett.100.136406
[65] K. Hu, M. Wu, S. Hinokuma, T. Ohto, M. Wakisaka, J.I. Fujita, Y. Ito, Boosting electrochemical water splitting: via ternary NiMoCo hybrid nanowire arrays, J. Mater. Chem. A 7 (2019) 2156–2164, https://doi.org/10.1039/c8ta11250a
[66] K. Parlinski, Phonon Code. ⟨http://wolf.ifj.edu.pl/phonon/⟩.
[67] F.J. Manjón, J. Angel, S. Tresserras, J. Ibáñez, A.L.J. Pereira, Pressure-induced phase transitions in sesquioxides, Crystals 9 (2019) 630, https://doi.org/10.3390/cryst9120630
[68] J. Zarembowitch, J. Gouteron, A.M. Lejus, Raman spectra of lanthanide sesquioxide single crystals with A-type structure, Phys. Status Solidi 94 (1979) 249–256, https://doi.org/10.1002/pssb.2220940128
[69] S. Jiang, J. Liu, L. Bai, X. Li, Y. Li, S. He, S. Yan, D. Liang, S. Jiang, J. Liu, L. Bai, X. Li, Y. Li, Anomalous compression behaviour in Nd_2O_3 studied by x-ray diffraction and Raman spectroscopy, AIP Adv. 8 (2018) 025019, https://doi.org/10.1063/1.5018020